



Structural effect of Ni/ZrO₂ catalyst on CO₂ methanation with enhanced activity

Xinyu Jia, Xiaoshan Zhang, Ning Rui, Xue Hu, Chang-jun Liu*

Tianjin Co-Innovation Center of Chemical Science & Engineering, School of Chemical Engineering and Technology, Tianjin University, Tianjin 300072, China



ARTICLE INFO

Keywords:
Ni/ZrO₂
Plasma
CO₂methanation
Ni(111)
Oxygen vacancy

ABSTRACT

A zirconia supported nickel catalyst for CO₂ methanation has been prepared via a rapid and effective plasma decomposition of nickel precursor at atmospheric pressure and temperature around 150 °C, followed by hydrogen reduction at 500 °C. The obtained Ni/ZrO₂ catalyst shows high Ni dispersion with principally exposed Ni (111) lattice plane. An enhanced cooperation between Ni and interfacial active sites is achieved as well, which leads to rapid dissociative adsorption of H₂ and hydrogen spillover. Sufficient H atoms are thereby generated for CO₂ hydrogenation and helpful to create oxygen vacancies on the ZrO₂ surface. Higher basicity correlated to the oxygen vacancies further enhances CO₂ adsorption and activation. Hence, a superior low temperature activity for CO₂ methanation was achieved. For example, a CO₂ conversion of 71.9% with a CH₄ yield of 69.5% was achieved over the plasma decomposed catalyst at 300 °C with a feeding gas consisting of H₂ (32 ml min⁻¹), CO₂ (8 ml min⁻¹) and N₂ (10 ml min⁻¹) at a GHSV of 60,000 h⁻¹. The corresponding TOF value towards CO₂ conversion is 0.61 s⁻¹. However, the CO₂ conversion, CH₄ yield and TOF value are only 32.9%, 30.3% and 0.39 s⁻¹ at the same reaction conditions over the thermally prepared catalyst. The *operando* DRIFT analyses demonstrate that CO₂ methanation over the plasma decomposed catalyst follows the CO-hydrogenation route. The exposed high-coordinate Ni(111) facets of the plasma decomposed catalyst facilitate the decomposition of CO₂ and formates into adsorbed CO. The subsequent hydrogenation of adsorbed CO leads to the production of methane. However, the thermally decomposed catalyst with complex Ni crystal structure and more defects mainly takes the pathway of direct formate hydrogenation. The present study confirms the structure of Ni/ZrO₂ has significant effect on the catalytic activity for CO₂ methanation.

1. Introduction

CO₂ utilization has attracted significantly increasing attentions worldwide [1,2]. Among various reactions exploited for CO₂ conversion and utilization, CO₂ hydrogenation to methane, or CO₂ methanation, provides us an effective approach to convert CO₂ in a large scale with high conversion at relatively mild conditions (like lower reaction temperatures compared to those for CO₂ reforming) [3–8]. The selectivity of methane can be very high (higher than 90%) with CO as the only by-product. Methane can be easily transported and stored with the existing natural gas infrastructures [9]. In addition, CO₂ methanation is also employed to support the life cycle system in the spacecraft [10,11]. It is an excellent candidate for the storage of renewable energy [11]. According to the literature survey, a remarkably increasing publication on the topic of CO₂ methanation has been recently observed.

Ni based catalyst has been extensively exploited for CO₂ methanation, because of its high activity and low price. However, in the

presence of CO as a by-product, the formation of Ni carbonyl species and deposited carbon on the Ni surface results in the catalytic instability and even deactivation [12,13]. Therefore, the design and preparation of Ni catalysts with low CO production and high carbon resistance is very necessary for practical applications. In addition, further improvement in the low-temperature activity for CO₂ methanation is a very important issue [14,15].

CO₂ methanation over Ni catalyst is structure sensitive. The catalyst size and structure have a remarkable influence on the catalytic performance [16–18]. The Ni-support interaction also has a significant influence on it [19]. The supporting material plays key roles not only in the dispersion of Ni catalysts but also in the promotion of CO₂ adsorption, activation and conversion [16]. SiO₂, MgO, Al₂O₃, TiO₂, CeO₂, ZrO₂ and many others have been exploited as the support for Ni catalysts in CO₂ methanation. Among these oxide supporting materials, the basic ZrO₂ shows superior properties with enhanced activity, high thermal stability and low carbon deposition rate, because of its rich

* Corresponding author.

E-mail address: coronacj@tju.edu.cn (C.-j. Liu).

surface active sites, basic sites (OH groups, adsorbed O^{2-}), acid-base $\text{Zr}^{4+}\text{-O}^{2-}$ pairs and oxygen vacancies [3,7,20]. Continuous efforts have been devoted in order to further improve the activity of Ni/ZrO_2 by using new catalyst preparation methods or adding various promoters. However, the low temperature activity of Ni/ZrO_2 still needs to be improved [4].

Recently, various gas discharge plasmas have been employed for the improvement in the catalyst preparation [21–23]. It has been found that the highly energetic electrons and excited species within the plasma cause a rapid decomposition of nickel nitrate and lead to the Ni catalysts with higher Ni dispersion (i.e., smaller Ni particle size), more exposed Ni(111) lattice planes and enhanced Ni-support interaction, as compared to the conventional thermal decomposition. Such prepared Ni catalysts have shown significantly improved activity for CO_2 methanation [10,15], CO methanation [24–26], dry reforming [9], steam reforming [27,28] and others. However, the effect of the plasma preparation on the oxygen vacancies needs to be investigated. In this work, we attempt to prepare a Ni/ZrO_2 catalyst for CO_2 methanation using the plasma decomposition of nickel nitrate. In addition to smaller Ni catalyst size and more Ni(111) achieved, we confirm that more oxygen vacancies at the Ni-ZrO_2 interface are formed with the plasma decomposition, leading to enhanced basic activity. An improved CO_2 adsorption has been achieved with further enhanced low temperature activity. The reaction mechanism for the plasma prepared Ni/ZrO_2 catalyst was discussed in detail.

2. Experimental

2.1. Catalyst preparation

Ni/ZrO_2 catalyst was prepared via incipient wetness impregnation method. ZrO_2 support was obtained from thermal calcination of $\text{Zr}(\text{NO}_3)_4$ (Tianjin Kemiou Chemical Reagent) at 500 °C for 3 h. The obtained ZrO_2 was first incipiently impregnated with an aqueous solution of $\text{Ni}(\text{NO}_3)_2\cdot6\text{H}_2\text{O}$ (Tianjin Kemiou Chemical Reagent) and then aged at ambient temperature for 12 h. After drying at 110 °C for another 12 h, one part of the impregnated sample ($\text{Ni}(\text{NO}_3)_2\cdot6\text{H}_2\text{O}/\text{ZrO}_2$) was calcined at 500 °C for 3 h. The acquired sample is denoted as $\text{NiO/ZrO}_2\text{-C}$. The other part of the impregnated sample was decomposed by using the dielectric barrier discharge (DBD) plasma for 1 h. The received sample was then carefully washed with de-ionized water and ethanol to remove undecomposed Ni ions [10]. The obtained sample is assigned as $\text{NiO/ZrO}_2\text{-P}$. Before reactions, the catalysts need to be reduced by H_2 at elevated temperature (with no use of the plasma). The obtained metallic Ni/ZrO_2 samples are assigned as $\text{Ni/ZrO}_2\text{-C}$ and $\text{Ni/ZrO}_2\text{-P}$.

The DBD setup used in this work has been described in details in our previous publications [24–28]. As a conventional gas discharge phenomenon for ozone generation, UV light and many others, the DBD plasma is here generated between two electrodes, separated by one or two insulating dielectric barriers (quartz plates in this work). A high voltage generator (CTP-2000 K; Corona Laboratory, Nanjing, China) was employed to create the plasma in argon atmosphere. The average voltage applied was 14 kV at a frequency of about 22 kHz with an average input power about 200 W. The DBD plasma decomposition was operated at the atmospheric pressure and the temperature around 150 °C, measured by infrared imaging (Ircon, 100PHT).

2.2. Characterization

77 K N_2 adsorption/desorption isotherms of the samples were measured on an AUTOSORB-1-C instrument (Quantachrome). The specific surface area (S_{BET}) and pore size distribution were calculated using the BET and DFT models, respectively. Total pore volume was obtained based on the adsorption volume at $P/P_0 = 0.99706$.

Thermogravimetric analyses (TG) were carried out on a Netzsch STA 449 F3 system with a heating rate of 10 °C min⁻¹ (from 35 to

1000 °C) under a flowing air of 25 ml min⁻¹.

X-ray powder diffraction (XRD) patterns were recorded by a Rigaku D/max-2500 diffractometer operated at 40 kV and 200 mA with Ni-filtered Cu target and $\text{K}\alpha$ ray irradiation. The scanning range of 2θ is from 10° to 90° at a scanning speed of 4° min⁻¹. Ni particle size was calculated with Scherrer equation based on the characteristic diffraction peaks.

Transmission electron microscopy (TEM) images were recorded using a Philips Tecnai G² F20 system equipped with an energy-dispersive X-ray spectrometer (EDX) operated at 200 kV. The fine powder was suspended into ethanol and then dispersed ultrasonically for 30 min. A drop of the suspension was deposited on a copper grid coated with carbon.

X-ray photoelectron spectroscopy (XPS) analyses were conducted on a Perkin Elmer PHI-1600 spectrometer using $\text{Mg K}\alpha$ ($h\nu = 1254 \text{ eV}$) radiation. The binding energies measured were calibrated with C1s peak (284.6 eV) as a reference.

H_2 temperature-programmed reduction ($\text{H}_2\text{-TPR}$) was conducted on a TPDRO 1100 apparatus (Thermo Finnigan, LLC). The sample (50 mg) was heated from room temperature to 900 °C at a rate of 10 °C min⁻¹ with a gaseous mixture of 5% H_2/N_2 at a flow rate of 30 ml min⁻¹. The effluent gas was analyzed by a thermal conductivity detector (TCD). CO_2 temperature-programmed desorption ($\text{CO}_2\text{-TPD}$) was carried out in a fixed-bed reactor. 100 mg of the sample was reduced with 8% H_2/N_2 (30 ml min⁻¹) at 500 °C for 1 h and then cooled to 50 °C, following CO_2 adsorption at 50 °C for 1 h. After purged with N_2 flow (30 ml min⁻¹) to remove physically adsorbed CO_2 , the sample was heated to 900 °C at a rate of 10 °C min⁻¹.

Operando diffuse reflectance infrared Fourier transform (DRIFT) spectroscopy was performed using a Tensor 27 spectrometer (Bruker) equipped with a MCT detector, by recording 32 scans at a resolution of 4 cm⁻¹. Prior to DRIFT measurements, the reduced sample needs to be reduced again at 400 °C for 1 h under a 5.0% H_2/Ar flow of 20 ml min⁻¹, followed by Ar purge (20 ml min⁻¹) for another 1 h, and then cooled to a desired temperature. The background spectra were firstly collected in the Ar atmosphere and subtracted from the sample spectra. For CO_2 adsorption, a 1.0% CO_2/Ar gas at the flow rate of 20 ml min⁻¹ was fed into the system at the temperature 50–350 °C with a heating rate of 10 °C min⁻¹. During the methanation reactions from 150 to 350 °C, the sample was exposed to the gas mixture (40 ml min⁻¹) containing 2.5% H_2 , 0.5% CO_2 (or CO) with Ar as carrier gas. The spectra were collected when a steady state was reached.

2.3. Activity test

CO_2 methanation was carried out in a quartz tubular fixed-bed reactor horizontally placed in a furnace under atmospheric pressure. 50 mg fresh catalyst (40–60 mesh) diluted with 100 mg silica carbide (40–60 mesh) loaded in the quartz tube was pre-reduced in situ by pure H_2 (20 ml min⁻¹) at 500 °C for 1 h. The reaction was conducted by feeding a gas mixture of H_2 (32 ml min⁻¹), CO_2 (8 ml min⁻¹) and N_2 (10 ml min⁻¹) in a temperature range of 200–400 °C with a gas hourly space velocity (GHSV) of 60,000 h⁻¹. The effluent was analyzed by an online gas chromatograph (Agilent 6890D), equipped with a thermal conductivity detector (TCD) and a Porapak Q column. CO_2 conversion (X_{CO_2}), CH_4 yield (Y_{CH_4}), CH_4 selectivity (S_{CH_4}), CO_2 conversion rate and space time yield (STY) of CH_4 were calculated according to the following equations:

$$X_{\text{CO}_2}(\%) = 100\% \times (F_{\text{CO}_2,\text{in}} - F_{\text{CO}_2,\text{out}})/F_{\text{CO}_2,\text{in}} \quad (1)$$

$$Y_{\text{CH}_4}(\%) = 100\% \times F_{\text{CH}_4,\text{out}}/F_{\text{CO}_2,\text{in}} \quad (2)$$

$$S_{\text{CH}_4}(\%) = 100\% \times F_{\text{CH}_4,\text{out}}/(F_{\text{CO}_2,\text{in}} - F_{\text{CO}_2,\text{out}}) \quad (3)$$

$$\text{CO}_2 \text{ conversion rate} = (X_{\text{CO}_2} \times F_{\text{CO}_2,\text{in}})/m_{\text{cat}} \quad (4)$$

$$\text{STY}_{\text{CH}_4} = \left(X_{\text{CO}_2} \times S_{\text{CH}_4} \times F_{\text{CO}_2,\text{in}} \right) / m_{\text{cat}} \quad (5)$$

where F_{in} and F_{out} are the molar flow rates of CO_2 or CH_4 at the entrance and the exit of the reactor, respectively. m_{cat} is the catalyst weight.

The turnover frequency (TOF) values towards CO_2 were defined as the number of CO_2 molecules converted over per surface metallic Ni active site per second [29]. The number of surface Ni sites was determined by Ni dispersion measured via TEM and CO chemisorption, assuming that one CO molecule was adsorbed on one single Ni site. TOF was calculated by the following equation:

$$\text{TOF}(\text{s}^{-1}) = \left(X_{\text{CO}_2} \times F_{\text{CO}_2,\text{in}} \right) / (m_{\text{cat}} \times M_s) \quad (6)$$

where M_s is the number of the surface Ni sites per gram catalyst.

3. Results and discussions

3.1. Catalytic activity of CO_2 methanation

Catalytic reaction of CO_2 methanation from 200 to 400 °C with the GHSV of 60,000 h⁻¹ has been performed over Ni/ZrO₂ catalysts. CO_2 conversion, CH_4 yield and CH_4 selectivity, used to evaluate catalytic activities, are presented in Fig. 1. Both catalysts possess almost 100% CH_4 selectivity at reaction temperature below 270 °C. Then a little by-product CO (with CO selectivity less than 4.1%) begins to be generated via the reverse water gas shift reaction (RWGS). The activity of Ni/ZrO₂-P increases as the temperature rises until 350 °C, with the highest CO_2 conversion of 79.1% and CH_4 yield of 76.5%. When the temperature reaches 400 °C, CO_2 conversion drops to 77.5% upon the limitation of the thermodynamic equilibrium conversion. For Ni/ZrO₂-C, CO_2 conversion and CH_4 yield can only reach up to 74.2% and 70.8%, respectively, at 400 °C. Besides, the activity of Ni/ZrO₂-P increases much more rapidly than Ni/ZrO₂-C at the temperature below 300 °C. For instance, Ni/ZrO₂-P presents a dramatically larger increase in CO_2 conversion from 15.4 to 50.2% than that of Ni/ZrO₂-C from 6.1 to 15.2%, when the temperature increases from 250 to 275 °C. TOF values towards CO_2 at 235 °C have been calculated based on Ni dispersion and listed in Table 1. Apparently, Ni/ZrO₂-P shows a higher TOF. These results indicate the superior low temperature activity of the Ni/ZrO₂-P catalyst.

Catalytic stability tests were also conducted at a GHSV of 60,000 h⁻¹ and a fixed temperature of 300 °C. As shown in Fig. S1 (see Supporting Materials), stable catalytic activities over both catalysts can be maintained for at least 600 min. CO_2 conversions of about 72.0% and 31.2% for Ni/ZrO₂-P and Ni/ZrO₂-C are very similar to those of

Table 1

Ni loading and dispersion of Ni/ZrO₂ catalysts and their TOF values based on CO_2 conversion.

Sample	Ni loading ^a (wt%)	Ni dispersion ^b (%)	Ni dispersion ^c (%)	TOF ^d (s ⁻¹)	TOF ^e (s ⁻¹)
Ni/ZrO ₂ -P	8.68	10.74	8.89	0.058	0.071
Ni/ZrO ₂ -C	10.00	6.24	5.58	0.040	0.045

^a Confirmed by ICP-MS measurement.

^b Calculated by Ni particle size from TEM.

^c Estimated from CO chemisorption by assuming that the ratio of CO to surface Ni atom is 1:1.

^d TOF of CO_2 conversion at 235 °C calculated based on TEM.

^e TOF of CO_2 conversion at 235 °C determined by CO chemisorption.

temperature-dependent activity tests in Fig. 1(a). Calculated on the basis of the steady-state activity at 300 °C, CO_2 conversion rate and STY of CH_4 for Ni/ZrO₂-P are 0.308 mol g_{cat}⁻¹ h⁻¹ and 0.301 mol g_{cat}⁻¹ h⁻¹, respectively, higher than those of the reported catalysts in the literature (Table S1). Most of the reported catalysts need higher reaction temperatures in order to get high activity. Ni/ZrO₂-P exhibits a significant improvement in the low temperature activity for CO_2 methanation. Table S2 further shows the comparison of TOF values of Ni catalysts towards CO_2 conversion (with CO_2 conversion less than 15% to ignore the potential effect of mass and heat transfer [30]). Ni/ZrO₂-P exhibits the highest TOF value, implying its higher intrinsic activity in CO_2 methanation.

3.2. Catalyst characterization

TG analyses have been performed to check the effectiveness of the DBD plasma decomposition. As shown in Fig. 2, the precursor Ni (NO₃)₂·xH₂O/ZrO₂ (i.e., the impregnated sample) shows a weight loss of 23.69% from 35 to 800 °C, which is attributed to the complete decomposition of nickel nitrate into nickel oxide. After the plasma decomposition, the obtained NiO/ZrO₂-P exhibits a weight loss of 4.51%. This indicates that the plasma can effectively decompose the nickel nitrate in the precursor [28].

Textural properties of the samples based on the N₂ adsorption-desorption measurements were evaluated, as shown in Table 2. The ZrO₂ support exhibits a mesoporous structure with 9.42 nm of average pore diameter and 75 m² g⁻¹ of BET surface area. Compared to NiO/ZrO₂-C, after Ni loading, NiO/ZrO₂-P exhibits less structural variation with smaller decreases in the surface area and average pore diameter. This is mainly because the plasma decomposition, as a rapid process at low temperature, is capable to inhibit Ni aggregation and diffusion, which

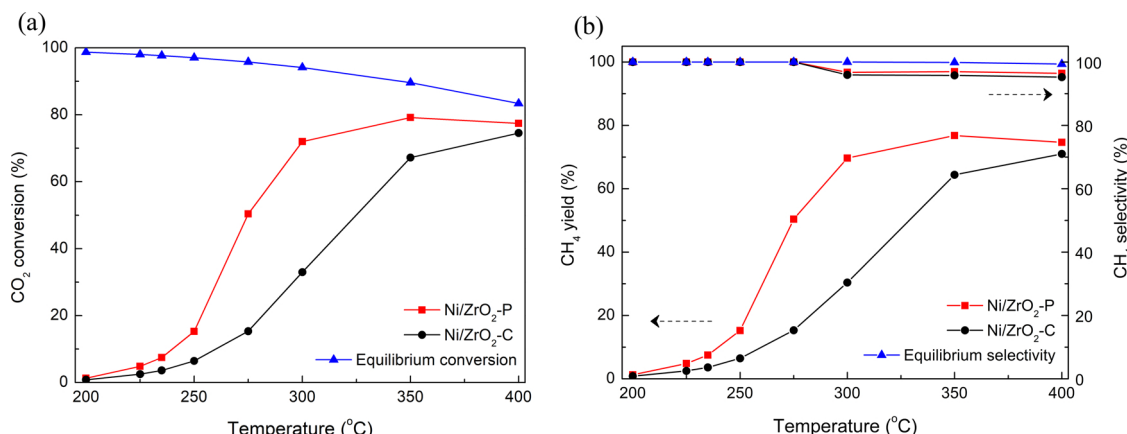


Fig. 1. (a) CO_2 conversion, (b) CH_4 yield and CH_4 selectivity of CO_2 methanation over Ni/ZrO₂-P and Ni/ZrO₂-C catalysts. Blue lines represent the thermodynamic equilibrium values of CO_2 conversion and CH_4 selectivity. (For interpretation of the references to colour in this figure legend, the reader is referred to the web version of this article).

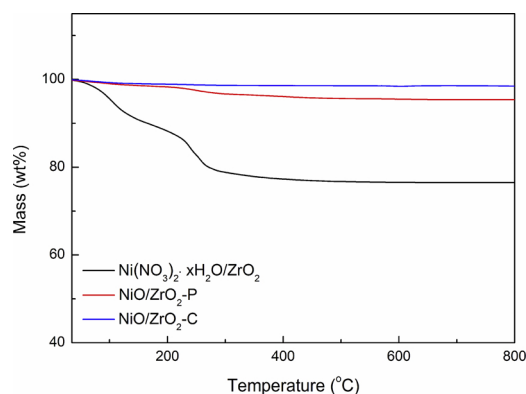


Fig. 2. TG curves of the Ni precursor ($\text{Ni}(\text{NO}_3)_2 \cdot x\text{H}_2\text{O}/\text{ZrO}_2$), $\text{NiO}/\text{ZrO}_2\text{-P}$ and $\text{NiO}/\text{ZrO}_2\text{-C}$ catalysts.

would block the pores of the support [15]. The better mesoporous structure of $\text{NiO}/\text{ZrO}_2\text{-P}$ is more beneficial for further adsorption and transfer of the reactants and intermediates during reactions.

XRD patterns of the fresh and reduced catalysts have been presented in Fig. 3. For all samples, the ZrO_2 support exists as a mixture of monoclinic (m) and tetragonal (t) phases. Diffraction peaks at 24.3° , 28.0° , 31.4° , 34.5° , 41.1° and 55.8° are assigned to m- ZrO_2 , and peaks at 30.4° , 35.5° , 50.5° and 60.3° are attributed to t- ZrO_2 . For $\text{NiO}/\text{ZrO}_2\text{-C}$, the peaks of $\text{NiO}(111)$ and (200) lattice planes located at 37.2° and 43.3° can be clearly identified. Nevertheless, no obvious NiO peaks can be found for $\text{NiO}/\text{ZrO}_2\text{-P}$, indicating that NiO nanoparticles are well dispersed on the support. Although $\text{Ni}(111)$ and (200) peaks at 44.7° and 51.8° are observed for both reduced samples, the peak of $\text{Ni}(111)$ in $\text{Ni}/\text{ZrO}_2\text{-C}$ is much sharper and stronger. Calculated via Scherrer equation on the basis of the $\text{Ni}(111)$ peaks, average Ni particle size of $\text{Ni}/\text{ZrO}_2\text{-C}$ is much larger than that of $\text{Ni}/\text{ZrO}_2\text{-P}$ (Table 2). These prove that the plasma decomposition plays a key role in enhancing Ni dispersion and reducing Ni particle size.

TEM images of both reduced samples are exhibited in Fig. 4(a) and (b). In each image, a large irregular feature on a lighter background can be observed, which is mainly attributed to the ZrO_2 support. Much smaller and darker areas within the support are assigned to metallic Ni nanoparticles. It can be seen that Ni particles over $\text{Ni}/\text{ZrO}_2\text{-P}$ are less agglomerative and more uniformly dispersed on the support than those over $\text{Ni}/\text{ZrO}_2\text{-C}$. Similar images were observed with the plasma decomposed Ni/SiO_2 catalyst [28]. As shown in Fig. S2, $\text{Ni}/\text{ZrO}_2\text{-P}$ displays a narrower Ni particle size distribution (from 4 to 12 nm) than $\text{Ni}/\text{ZrO}_2\text{-C}$ (from 6 to 26 nm), supporting more homogeneous Ni dispersion of $\text{Ni}/\text{ZrO}_2\text{-P}$. Ray and Deo [29] used the same way to analyze $\text{Ni}/\text{Al}_2\text{O}_3$ catalyst for CO_2 methanation. In Table 2, the average Ni particle size of $\text{Ni}/\text{ZrO}_2\text{-P}$ is 9.31 nm, smaller than that of $\text{Ni}/\text{ZrO}_2\text{-C}$ (16.03 nm). This agrees well with the XRD results. High resolution TEM images in Fig. 4(c) and (e) exhibit well-defined $\text{Ni}(111)$ lattice fringes on $\text{Ni}/\text{ZrO}_2\text{-P}$. Both m- $\text{ZrO}_2(111)$ and t- $\text{ZrO}_2(111)$ fringes can be observed clearly. Nevertheless, the Ni facets on $\text{Ni}/\text{ZrO}_2\text{-C}$ are difficult to be

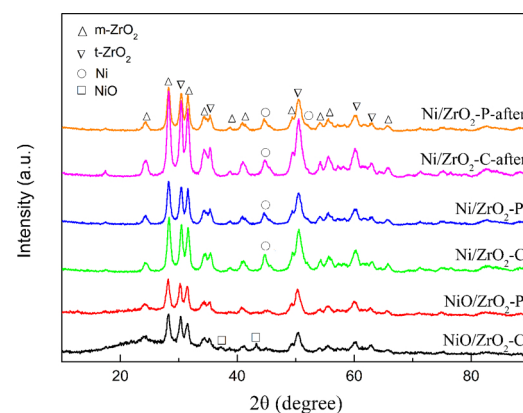


Fig. 3. XRD patterns of the fresh, reduced and used Ni/ZrO_2 catalysts.

distinguished owing to the highly disordered crystal structure of the Ni particles. Compared with the plasma treatment, the higher-temperature thermal effect contributes to the anisotropic growth of Ni with the multi-faceted structure enriching defect sites [24,25]. Combined with the XRD results, the TEM image of used $\text{Ni}/\text{ZrO}_2\text{-C}$ catalyst in Fig. 4(g) reveals serious agglomeration of Ni into larger particles up to 30–40 nm, ascribed to high-temperature sintering effect. For the used $\text{Ni}/\text{ZrO}_2\text{-P}$, most of the Ni particles are still homogeneously dispersed with no significant size growth (Fig. 4(f)). No obvious Ni particle growth of $\text{Ni}/\text{ZrO}_2\text{-P}$ reflects its superior sintering resistance, attributed to the intense interaction between Ni and ZrO_2 support [27,28].

The reduction behaviors of NiO and ZrO_2 have been investigated using $\text{H}_2\text{-TPR}$ as shown in Fig. 5. The overlapping peaks were fitted by a Gaussian-type function to figure out the different types of oxide species. NiO reduction at low or high temperatures deeply depends on its size and the degree of interaction with the support. Highly dispersed Ni particles in stronger interaction with the support are generally reduced at higher temperatures [13]. It is clear that the plasma decomposition shifts reduction temperatures towards higher values as compared with the calcination method. Seven fitting peaks were separated for the $\text{Ni}/\text{ZrO}_2\text{-C}$ catalyst, while only five peaks were obtained for $\text{Ni}/\text{ZrO}_2\text{-P}$. This implies more uniform Ni distribution on the $\text{Ni}/\text{ZrO}_2\text{-P}$ surface. The small shoulder peaks located at 240°C and 255°C are assigned as the reduction of unsupported Ni on $\text{Ni}/\text{ZrO}_2\text{-C}$ [31]. The peaks at 296°C and 315°C belong to Ni particles weakly contacting with ZrO_2 . These two types of Ni on $\text{Ni}/\text{ZrO}_2\text{-P}$ significantly decrease, as evidenced by smaller peak areas at 297°C and 328°C . On the contrary, $\text{Ni}/\text{ZrO}_2\text{-P}$ possesses more Ni species strongly interacting with ZrO_2 , as supported by larger peak areas at 355°C and 393°C than those at 352°C and 405°C for $\text{Ni}/\text{ZrO}_2\text{-C}$. The higher temperature peaks, centered at 476°C (for $\text{Ni}/\text{ZrO}_2\text{-P}$) and 492°C (for $\text{Ni}/\text{ZrO}_2\text{-C}$), have been proposed to be the reduction of ZrO_2 at the Ni-ZrO_2 interface by spillover hydrogen [32,33].

Once reduced, Ni active sites can adsorb and dissociate H_2 into H atoms which move towards the ZrO_2 surface and react with oxidative species. The stronger Ni-ZrO_2 interaction over $\text{Ni}/\text{ZrO}_2\text{-P}$ enhances the

Table 2
Textural properties and H_2 consumption of the support and the catalysts.

Sample	$S_{\text{BET}}^{\text{a}}$ (m^2g^{-1})	V_p^{a} (cm^3g^{-1})	D ^a (nm)	Ni particle size ^b (nm)	Ni particle size ^c (nm)	H_2 consumption ^d (mmol g^{-1})
ZrO_2	75	0.24	9.42	-	-	-
$\text{NiO}/\text{ZrO}_2\text{-P}$	70	0.24	8.13	10.58	9.31	2.61
$\text{NiO}/\text{ZrO}_2\text{-C}$	52	0.20	7.45	18.30	16.03	2.13

^a S_{BET} , V_p and D represented BET surface area, total pore volume and average pore diameter measured by N_2 adsorption-desorption at 77 K.

^b Calculated by Scherrer equation based on the $\text{Ni}(111)$ diffraction peak decided by XRD measurement.

^c Derived from TEM particle size distribution.

^d Determined by $\text{H}_2\text{-TPR}$ measurement.

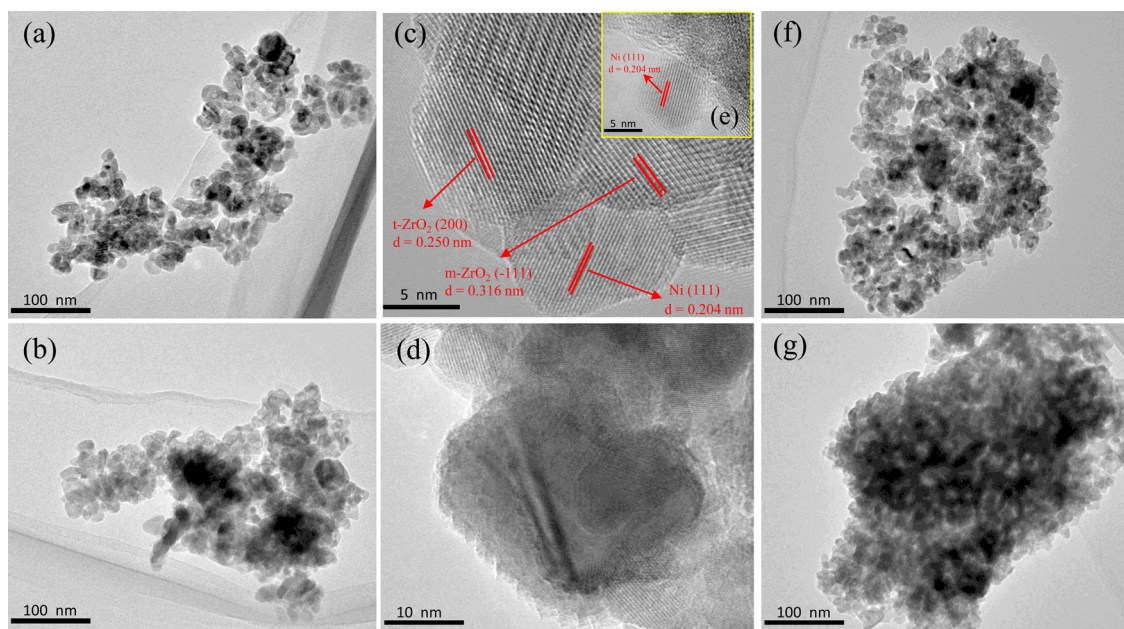


Fig. 4. TEM images of (a) Ni/ZrO₂-P, (b) Ni/ZrO₂-C, (f) used Ni/ZrO₂-P and (g) used Ni/ZrO₂-C; high-resolution TEM images of (c) (e) Ni/ZrO₂-P and (d) Ni/ZrO₂-C.

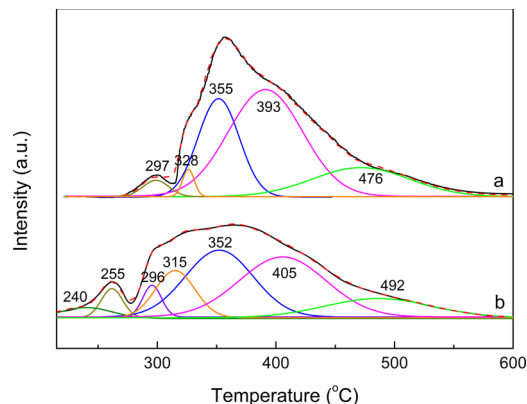


Fig. 5. H₂-TPR profiles of Ni/ZrO₂-P (a) and Ni/ZrO₂-C (b) catalysts.

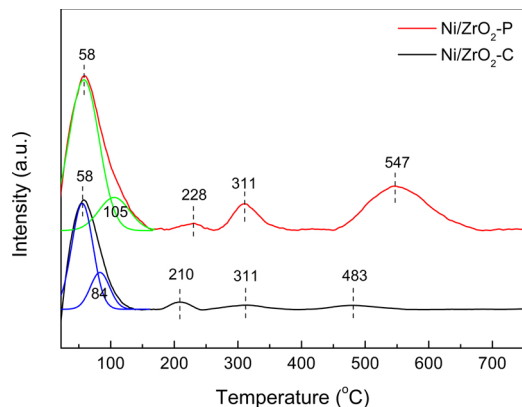


Fig. 6. CO₂-TPD curves of Ni/ZrO₂-P and Ni/ZrO₂-C catalysts.

hydrogen spillover, and further increases the ZrO₂ reduction at lower temperature [34,35]. If assuming that all the H₂ consumption was attributed to the NiO reduction, the calculated Ni loading amounts in Ni/ZrO₂-P and Ni/ZrO₂-C are 15.03% and 12.13%, much higher than the actual amounts of 8.68% and 10.00% determined by ICP-MS measurements (Table 1). The additional H₂ uptake should be associated to the ZrO₂ reduction. In addition to OH groups and adsorbed O²⁻ species, surface lattice oxygen should be reduced along with the formation of oxygen vacancies [34,35]. Apparently, the partial reduction of ZrO₂ over Ni/ZrO₂-P is more pronounced, compared to Ni/ZrO₂-C. More oxygen vacancies will be produced as unique interfacial active sites [36,37].

CO₂-TPD characterization was performed to examine the surface basicity of Ni/ZrO₂ catalysts. Desorption peaks relate to the interaction of acidic CO₂ with the ZrO₂ basic sites in distinguishing strengths. As shown in Fig. 6, four peaks for both catalysts can be clearly observed, which have been proposed to represent different (bi)carbonate species formed from CO₂ adsorption on the basic sites. The most intense signal at 58 °C can be assigned to the physically adsorbed CO₂ [38]. The peaks in 80–150 °C are ascribed to the weakly basic sites provided by surface OH groups, related to bicarbonate species. Acid-base Zr⁴⁺-O²⁻ pairs mainly serve as moderately basic sites, which appear in 150–300 °C. Higher temperature peaks from 300 to 700 °C are associated with

strongly basic adsorbed O²⁻ species [39–41]. Combining DRIFT with CO₂-TPD studies on the ZrO₂ basicity, Pokrovski et al. [42] demonstrated that CO₂ desorption from moderately and strongly basic sites corresponded to the decomposition of bidentate and monodentate carbonates, respectively. Pan et al. [43] proved that the adsorbed O²⁻ sites, associated with the CO₂ desorption from 300 to 700 °C, significantly promoted the formation of monodentate carbonates and the subsequent hydrogenation to monodentate formates and finally to gaseous CH₄. As a result, the much larger peaks at 311 and 547 °C for Ni/ZrO₂-P, than those at 311 and 483 °C for Ni/ZrO₂-C, imply the remarkably enhanced CO₂ adsorption capacity with more monodentate carbonate formation on Ni/ZrO₂-P. Drouilly et al. [44] emphasized that oxygen vacancy concentration was positively correlated with the basic reactivity of the adsorbed O²⁻ sites. The electronic density of these active sites would deeply depend on the formation or filling up of oxygen vacancies with electron release or capture. Activated CO₂ can provide the adsorbed O²⁻ species by replenishing oxygen vacancies with adsorbed CO release [32]. In a word, the strongly basic adsorbed O²⁻ formation caused by the increase of oxygen vacancies is one of the reasons for the significantly enhanced activity of Ni/ZrO₂-P in CO₂ methanation.

XPS analyses were conducted to explore the influence of the plasma decomposition on the electronic structure of Ni/ZrO₂ catalysts. The Ni

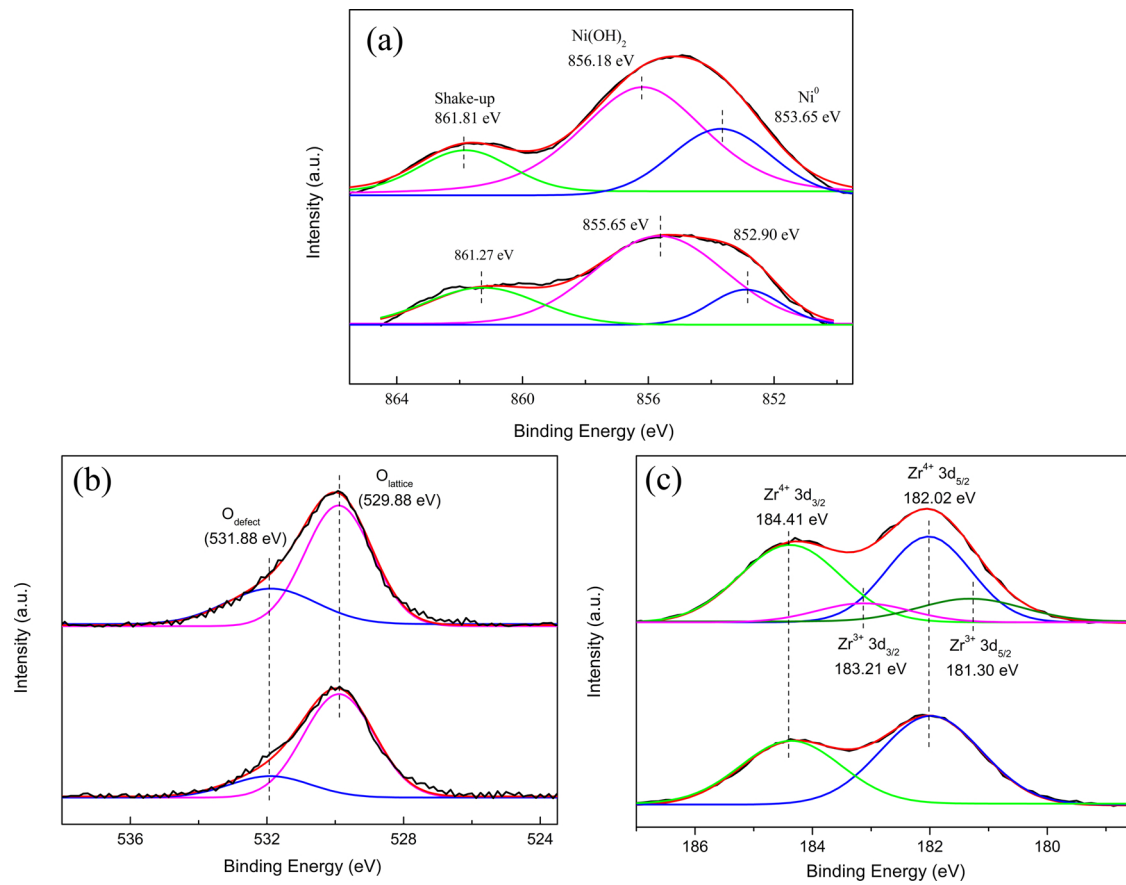


Fig. 7. XPS spectra of (a) Ni 2p_{3/2}, (b) O 1 s, and (c) Zr 3d over Ni/ZrO₂-P (top) and Ni/ZrO₂-C (bottom) catalysts.

2p_{3/2} spectra in Fig. 7(a) show that the Ni catalysts mainly consist of Ni in metallic, oxidic and hydroxidic forms [45,46]. The oxidic Ni²⁺ formation is mainly due to the exposure of the catalyst to air. Three peaks at 853.65, 856.18 and 861.81 eV for Ni/ZrO₂-P can be attributed to Ni⁰/NiO, Ni(OH)₂, and shake-up satellite peak, respectively [47,48]. The slight shift of Ni 2p_{3/2} binding energies for Ni/ZrO₂-C towards lower values suggests the larger size of Ni particles [49]. The surface Ni concentration of Ni/ZrO₂-P, estimated by Ni/Zr = 0.18, is higher than that of Ni/ZrO₂-C (Ni/Zr = 0.13). This indicates a better Ni dispersion on the support induced by the plasma decomposition.

In Fig. 7(c), the XPS spectrum of Ni/ZrO₂-P shows the peaks of Zr 3d_{3/2} and Zr 3d_{5/2} centered at 184.41 eV and 182.02 eV, which are assigned to Zr⁴⁺ state for ZrO₂. The existence of two other peaks with lower binding energies of 183.21 eV and 181.30 eV suggests the partial reduction of Zr⁴⁺ towards Zr^{x+} (x < 4) [39,50]. Unlike Ni/ZrO₂-P, it is difficult to distinguish Zr^{x+} 3d peaks for Ni/ZrO₂-C. The O 1 s core level spectra in Fig. 7(b) exhibit two peaks for both samples. The peak at 529.88 eV originates from the lattice oxygen of ZrO₂ (O_{lattice}), and the minor peak at the higher binding energy of 531.88 eV normally belongs to oxygen anions on the oxygen-deficient ZrO_{x/2} surface (O_{defect}) [38,51]. The relative concentrations of the oxygen vacancies (C_{Odefect}) calculated based on the formula of C_{Odefect} = A_{Odefect}/(A_{Odefect} + A_{Olattice}) (A expressed as the peak area) are 28.2% and 15.1% for Ni/ZrO₂-P and Ni/ZrO₂-C, respectively. This result combined with the discovery of Zr^{x+} species demonstrates that Ni/ZrO₂-P facilitates the partial reduction of ZrO₂ to create more oxygen vacancies.

3.3. Discussions

3.3.1. Operando DRIFT analyses

To obtain deep insight into the mechanisms of CO₂ methanation

over both Ni-ZrO₂ catalysts, *operando* DRIFT analyses have been carried out under CO₂, CO₂/H₂ and CO/H₂ gas mixtures. The evolution of the surface species during CO₂ adsorption and hydrogenation can be monitored.

3.3.1.1. CO₂ adsorption. Fig. 8(a) presents *operando* DRIFT spectra, following the condition of the temperature-programmed CO₂ adsorption over Ni/ZrO₂-P in the temperature range of 50–350 °C. At 50 °C, the appearance of bands at 1625, 1416 and 1220 cm⁻¹ is attributed to bidentate bicarbonate species. The band at 1335 cm⁻¹ can be assigned to monodentate carbonates. As the temperature increases, the band intensities for the bicarbonates decrease monotonically. However, new bands for bidentate formates (1572 and 1356 cm⁻¹), bidentate carbonates (1552, 1537 and 1320 cm⁻¹) and monodentate carbonates (1521, 1450 and 1335 cm⁻¹) appear and gradually increase. Meanwhile, monodentate carbonates increase more rapidly than bidentate carbonates above 200 °C, implying their better thermal stability. Combined with the above CO₂-TPD results, these DRIFT phenomena verify that OH groups on the ZrO₂ surface provide weakly basic sites for bicarbonates, whereas acid-base Zr⁴⁺-O²⁻ pairs and adsorbed O²⁻ sites serve as moderately and strongly basic sites for bidentate and monodentate carbonates. A summary of the assignments of the bands for (bi)carbonate and formate species is shown in Table 3 [3,42,43,52–55].

It is worth noting that the bands related to adsorbed CO (CO_{ads}) in linear and bridge forms on the Ni surface are visible in 2100–1950 cm⁻¹ and 1950–1750 cm⁻¹, respectively. The adsorbed CO should be formed from direct CO₂ dissociation (CO_{2(ads)} → CO_(ads) + O_(ads)) on the Ni(111) facets, followed by the reaction with OH groups towards a small amount of formates (CO_{ads} + OH_{ads} → HCOO_{ads}) [56]. The appearance of the bands for bidentate formates is a good evidence

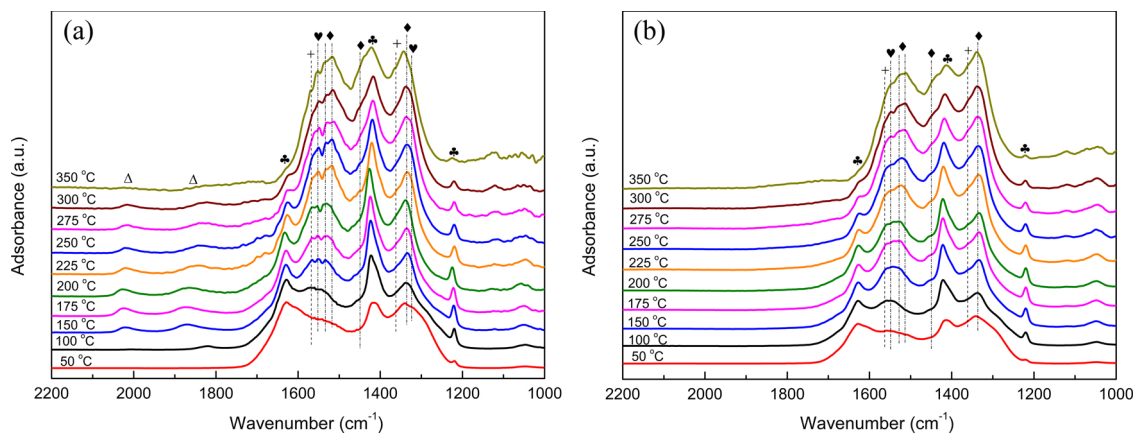


Fig. 8. Operando DRIFT spectra during temperature-programmed CO₂ adsorption in a 1.0% CO₂/Ar gas at the flow rate of 20 ml min⁻¹ with a heating rate of 10 °C min⁻¹ over Ni/ZrO₂-P (a) and Ni/ZrO₂-C (b). Every spectrum at the desired temperatures (50–350 °C) was collected when CO₂ adsorption reached a steady state. Symbol definition: bidentate bicarbonate (♣), monodentate carbonates (♦), bidentate formate (♥), bidentate formate (+), linear CO or bridge CO (△).

Table 3

Observed infrared vibrational frequencies (cm⁻¹) for (bi)carbonate and formate species on Ni/ZrO₂ samples in CO₂ adsorption and methanation.

Surface species	Assignment	Frequencies (cm ⁻¹)		Refs.
		Ni/ZrO ₂ -P	Ni/ZrO ₂ -C	
Bicarbonate		ν_{as} (CO ₃) ν_s (CO ₃) δ (OH)	1625 1416 1220	[3,52]
Monodentate carbonate		ν_{as} (CO ₃) ν_{as} (CO ₃) ν_s (CO ₃)	1521 1450 1335	[42,43]
Bidentate carbonate		ν_{as} (CO ₃) ν_{as} (CO ₃) ν_s (CO ₃)	1552 1537 1320	[52,53]
Bidentate formate		ν (CH) ν_{as} (CO ₂) δ (CH) ν_s (CO ₂)	2867 1572 1384 1356	[54,55]
Monodentate formate		ν_{as} (CO ₂) ν_s (CO ₂)	1610 1332	[42,52]

for the CO₂ dissociation. Using ambient-pressure X-ray photoelectron spectroscopy (AP-XPS), Heine et al. [46] have demonstrated that the Ni (111) surface facilitates the dissociation of CO₂ into adsorbed CO as a crucial intermediate for CH₄ synthesis. The DFT studies confirmed it as well [57,58]. As shown in Fig. 8(b), a negligible amount of adsorbed CO and weaker band intensities of formates can be observed for Ni/ZrO₂-C, suggesting the suppression of the CO₂ dissociation on the complex and multi-faceted Ni surface enriching defects. The (bi)carbonate species with almost the same vibrational frequencies as those on Ni/ZrO₂-P are also visible. However, their lower intensities strongly support that there are less basic sites on the Ni/ZrO₂-C surface responsible for CO₂ adsorption and activation.

3.3.1.2. CO₂ methanation. Operando DRIFT measurements for CO₂ methanation over Ni/ZrO₂ catalysts were also conducted as presented in Fig. 9. At 150 °C, the typical CO₂ adsorption species, including bicarbonates (1625, 1416 and 1220 cm⁻¹), monodentate carbonates (1521, 1450 and 1335 cm⁻¹) and bidentate formates (2867, 1572, 1384 and 1356 cm⁻¹), can be observable for Ni/ZrO₂-P in Fig. 9(a). Bidentate formates keep substantially increasing up to 200 °C, accompanied by the decrease of both bidentate bicarbonates and

monodentate carbonates. However, bidentate carbonates are invisible due to their instability and rapid decomposition before hydrogenation to formates [43]. Noteworthy is the appearance of a shoulder band at 1610 cm⁻¹, which is typically attributed to monodentate formates. It has been proposed that bidentate formates originate from the hydrogenation of bidentate bicarbonates, and monodentate formates are derived from the hydrogenation of monodentate carbonates [43,54]. Korhonen et al. [53] theoretically proved that monodentate formates were also key intermediates for CH₄ production, but their lower stability and higher reactivity made them difficult to be detected. Operando DRIFT spectra for formic acid hydrogenation conducted by Pan et al. [43] exhibited the formation of both types of formates and the much faster conversion of monodentate formates towards CH₄. Hence, a smaller amount of monodentate formates left on Ni/ZrO₂-P is mainly owing to their faster hydrogenation and decomposition. Fig. 9(b) shows that bidentate formates start to be formed apparently at 175 °C on Ni/ZrO₂-C, and their generation rate is far lower than that on Ni/ZrO₂-P. The negligible amount of monodentate formates implies less monodentate carbonate formation from CO₂ adsorption on the adsorbed O²⁻ sites. It can be sure that Ni/ZrO₂-P significantly improves the activity of the (bi)carbonate hydrogenation towards bidentate and monodentate formates.

In order to describe the evolution of adsorbed and gaseous species in function of the temperature, the relative concentrations of bidentate formates and adsorbed CO as well as gaseous CH₄ have been calculated based on the operando DRIFT results, as shown in Fig. 10. The quantification of adsorbed CO was made by the integration of bands in the range of 2100–1750 cm⁻¹, while the quantifications of formates and CH₄ were made following the band intensities at 1572 and 3015 cm⁻¹ [56]. The highest value measured for every species was set to 100.0% in order to obtain normalized relative concentrations from 200 to 350 °C. For Ni/ZrO₂-P in Fig. 10(a), with the increasing temperature from 200 to 250 °C, a gradual decrease of formates is caused from 100.0 to 70.1%, accompanied by the respective increase of adsorbed CO and CH₄ from 20.9 to 64.6% and 1.6 to 17.2%. These variations bring evidence that the dissociation of formates into adsorbed CO is dominant for formate conversion at first. Above 250 °C, the CH₄ production rate is significantly boosted by the hydrogenation steps. The adsorbed CO reaches the maximum at 275 °C, and then begins to be consumed to form CH₄. Considering the respective evolution of adsorbed CO and CH₄ with the temperature, it is reasonable that the CH₄ production is mainly limited by the rate-limiting steps of CO dissociation and hydrogenation [56]. In addition, CO₂ methanation over Ni/ZrO₂-P prefers to proceed via the direct hydrogenation of formates (formate_(ads) → CH_{4(g)}) and the formate dissociation followed by the hydrogenation of adsorbed CO (formate_(ads) → CO_(ads) → CH_{4(g)}). In Fig. 10(b), Ni/ZrO₂-C

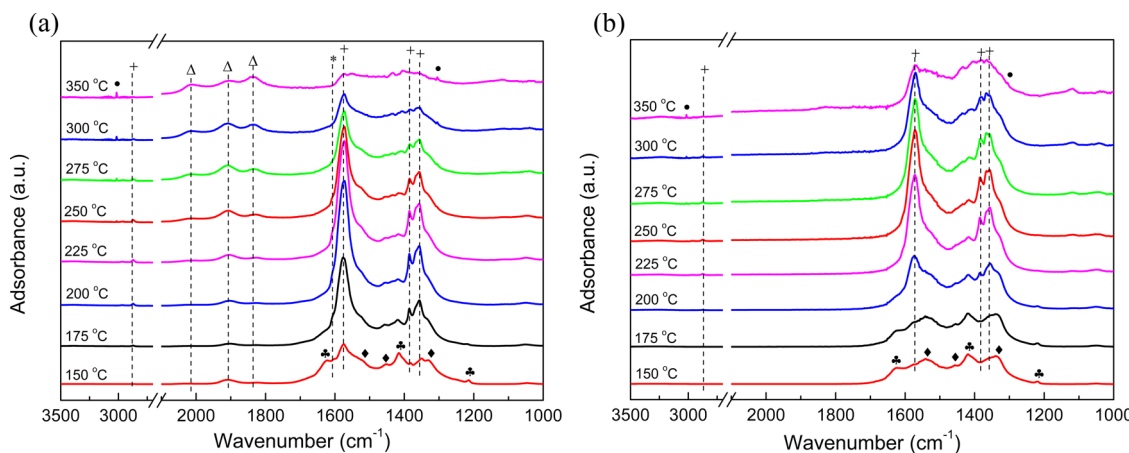


Fig. 9. *Operando* DRIFT spectra during temperature-programmed reaction of a gas mixture (40 ml min^{-1}) containing 2.5% H_2 , 0.5% CO_2 with Ar as carrier gas over Ni/ZrO₂-P (a) and Ni/ZrO₂-C (b). The heating rate is $10 \text{ }^{\circ}\text{C min}^{-1}$. Symbol definition: bidentate bicarbonate (●), monodentate carbonates (◆), bidentate formate (+), monodentate formate (*), linear CO or bridge CO (Δ) and gaseous CH₄ (●).

exhibits the highest concentration of bidentate formates at $250 \text{ }^{\circ}\text{C}$, and CH₄ gets produced rapidly from the higher temperature of $275 \text{ }^{\circ}\text{C}$. This indicates the lower activity of the formate formation and further hydrogenation over Ni/ZrO₂-C catalyst, compared to Ni/ZrO₂-P. The suppression of the formate dissociation into adsorbed CO reveals that Ni/ZrO₂-C keeps a direct formate hydrogenation pathway for the CH₄ synthesis.

To verify the difference of the formate conversion between two Ni/ZrO₂ samples, the DRIFT spectra of higher-temperature desorption of adsorbed species formed from CO₂ methanation at $225 \text{ }^{\circ}\text{C}$ were measured (Fig. S3). As a principal intermediate species formed on Ni/ZrO₂-P at $225 \text{ }^{\circ}\text{C}$, bidentate formates can be largely decomposed into gaseous CH₄ as well as adsorbed CO (especially the bridge type) above $275 \text{ }^{\circ}\text{C}$. In contrary, less bidentate formates with lower band intensities are displayed on Ni/ZrO₂-C, and a higher desorption temperature of $300 \text{ }^{\circ}\text{C}$ is required for the sufficient formate conversion into CH₄ and little adsorbed CO. It appears that the plasma decomposition indeed changes the reaction pathway from formate-hydrogenation route to CO-hydrogenation route by favoring the formate dissociation into adsorbed CO on the Ni(111) surface.

3.3.1.3. CO methanation. To make a further discussion for the CO-hydrogenation pathway, *operando* DRIFT of CO methanation has been performed, as shown in Fig. 11. Bidentate formates as the main adsorbed species are obtained from the interaction between CO and OH groups on the ZrO₂ surface. What is clear is that adsorbed CO

species on Ni/ZrO₂-P presents distinct profiles from those on Ni/ZrO₂-C. Bridge-bound CO ($1950\text{--}1750 \text{ cm}^{-1}$) is associated to CO adsorption on the close-packed Ni(111) sites, whereas linear-bound CO ($2100\text{--}1950 \text{ cm}^{-1}$) refers to CO connected on Ni defect sites [24]. It is noted that the relative population of two types of adsorbed CO keeps changing with the temperature. From 150 to $240 \text{ }^{\circ}\text{C}$, the bridge CO on Ni/ZrO₂-P consistently increases at the expense of the linear CO. This is mainly owing to that the less stable adsorption of the linear CO on the Ni defect sites results in CO transfer towards the Ni(111) sites as a more stable bridge form. Above $240 \text{ }^{\circ}\text{C}$, the most part of bidentate formates can be converted into bridge CO as well as gaseous CH₄. Therefore, it is reasonable that CO₂ methanation on Ni/ZrO₂-P with the enriched Ni (111) facets favorably follows the formate decomposition followed by CO hydrogenation route, involving the bridge–CO formation, migration and hydrogenation [55]. Much less bridge–CO formed on Ni/ZrO₂-C is due to the existence of less Ni(111) sites with more defects. Ni/ZrO₂-C fails to promote the formate dissociation and stabilize the adsorbed CO, leading to a formate-hydrogenation pathway for CO₂ methanation.

Based on our studies, we propose that CO₂ methanation on Ni/ZrO₂-P takes place via a CO-route as schematically summarized in Fig. 12(a). Over the Ni-ZrO₂ interface, gaseous CO₂ reacts with OH groups and adsorbed O²⁻, giving bidentate bicarbonates and monodentate carbonates, respectively. The adsorbed O²⁻ sites inserted into the oxygen vacancies are most plausibly formed by CO₂ chemisorption and dissociation [54–56]. Gaseous H₂ is adsorbed on Ni particles and

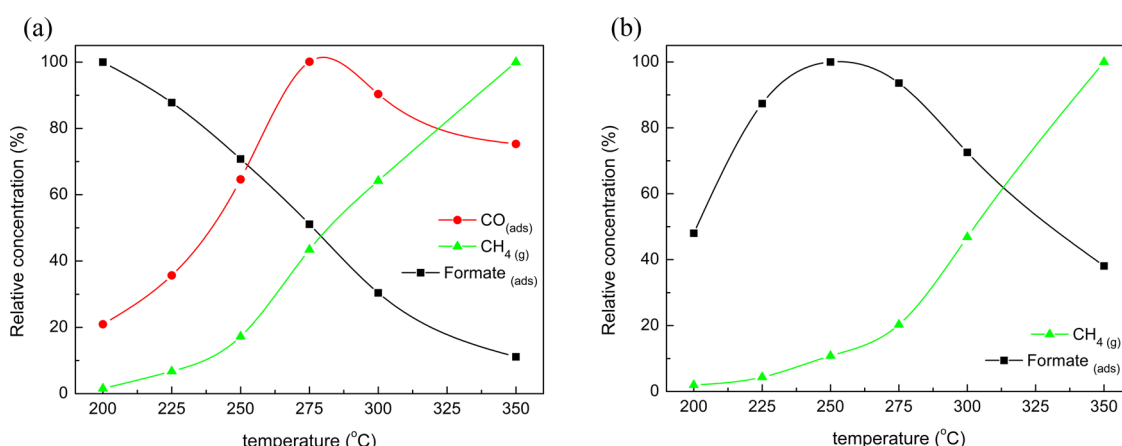


Fig. 10. Variation of relative concentrations of CH₄_(g) (3015 cm^{-1}), adsorbed CO ($2100\text{--}1750 \text{ cm}^{-1}$) and bidentate formates (1572 cm^{-1}) during temperature-programmed CO₂ methanation over Ni/ZrO₂-P (a) and Ni/ZrO₂-C (b).

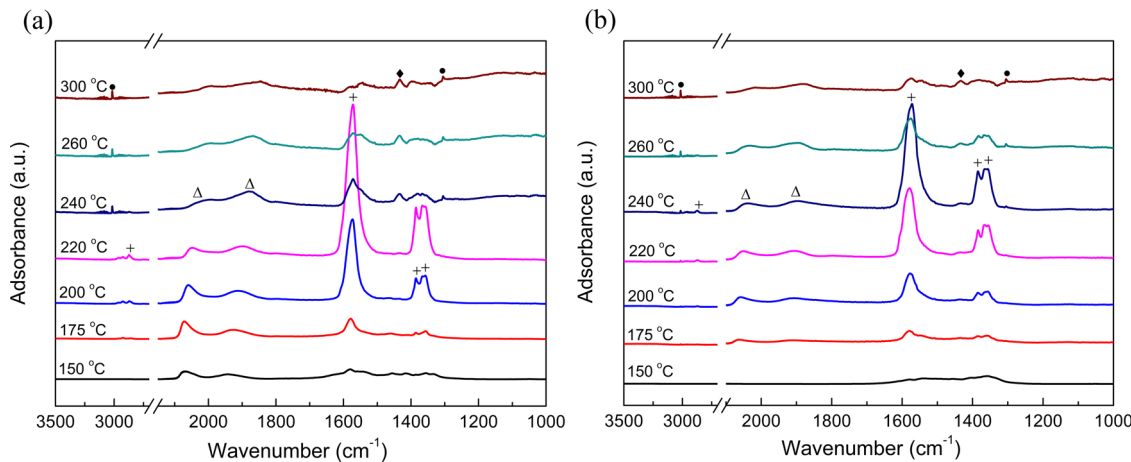


Fig. 11. Operando DRIFT spectra during temperature-programmed reaction of a gas mixture (40 ml min^{-1}) containing 2.5% H_2 , 0.5% CO with Ar as carrier gas over $\text{Ni}/\text{ZrO}_2\text{-P}$ (a) and $\text{Ni}/\text{ZrO}_2\text{-C}$ (b). The heating rate is $10 \text{ }^{\circ}\text{C min}^{-1}$. Symbol definition: monodentate carbonates (◆), bidentate formate (+), linear CO or bridge CO (△) and gaseous CH_4 (●).

dissociated into H atoms which can rapidly diffuse via a spillover process. These H atoms react with (bi)carbonates to produce bidentate/monodentate formates and water. Then, the formates are decomposed into adsorbed CO that moves towards the Ni(111) sites and is bound in a stable bridge form. Final product CH_4 is mainly formed from the CO hydrogenation on the Ni surface. In contrary, the reaction pathway of $\text{Ni}/\text{ZrO}_2\text{-C}$ takes a formate route as represented in Fig. 12(b). Surface OH groups serve as the principally active sites for CO_2 adsorption and activation, owing to the lack of the adsorbed O^{2-} sites. Bidentate bi-carbonates and formates are the adsorption and intermediate species, respectively, and subsequent hydrogenation of the formates is a critical synthetic path for CH_4 .

3.3.2. Kinetic studies

Kinetic studies have been further conducted for the comparison of kinetic parameters of $\text{Ni}/\text{ZrO}_2\text{-P}$ and $\text{Ni}/\text{ZrO}_2\text{-C}$ catalysts under differential reactor conditions with CO_2 conversion below 15% [59]. The apparent activation energies for CO_2 methanation were calculated by Arrhenius plots, as shown in Fig. S4. CO_2 conversion rates (r_{CO_2}) for the calculation of reaction rate constants (k) in Arrhenius plots were determined by the Eq. (4). Apparent reaction orders were determined by the slopes of the fitted $\ln r_{\text{CO}_2} \sim \ln P$ lines in Fig S5. As exhibited in Table S3, the apparent activation energy of $\text{Ni}/\text{ZrO}_2\text{-P}$ is $93.61 \text{ kJ mol}^{-1}$,

which is almost the same as that of $\text{Ni}/\text{ZrO}_2\text{-C}$ ($93.12 \text{ kJ mol}^{-1}$). The different reaction orders for CO_2 and H_2 suggest the different dependence degrees of the reaction rates on CO_2/H_2 concentrations between two catalysts. These imply different reaction pathways over two catalysts for CO_2 hydrogenation with similar apparent energy barriers. The pre-exponential factor for $\text{Ni}/\text{ZrO}_2\text{-P}$ is $2.48 \times 10^{10} \text{ L g}^{-1} \text{ h}^{-1}$, whereas it is only $6.93 \times 10^9 \text{ L g}^{-1} \text{ h}^{-1}$ for $\text{Ni}/\text{ZrO}_2\text{-C}$. This strongly supports that a greater number of active sites can be provided by highly dispersed Ni particles on $\text{Ni}/\text{ZrO}_2\text{-P}$, leading to higher reaction rate for CO_2 methanation [60,61].

In a word, the excellent structural properties of the plasma-decomposed catalyst indeed cause a superior catalytic performance. The principally exposed Ni(111) surface facilitates the formate dissociation and adsorbed CO stabilization, which leads to a CO-hydrogenation mechanism for CO_2 methanation. Higher Ni dispersion with smaller particle size contributes to a better ability for the dissociated adsorption of H_2 , thereby supplying more H atoms for the hydrogenation and creation of oxygen vacancies. Higher basic reactivity of ZrO_2 correlated to higher oxygen vacancy concentration effectively improves the CO_2 adsorption and activation. Above all, the stronger Ni-ZrO₂ interaction accelerates the hydrogen spillover and CO migration in the interfacial region.

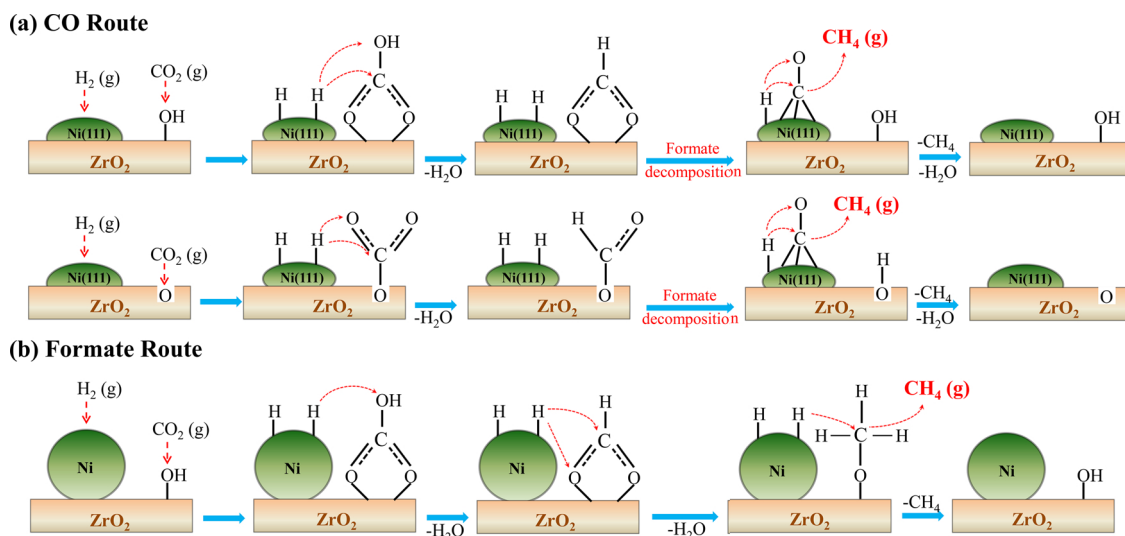


Fig. 12. Proposed pathway for CO_2 methanation over $\text{Ni}/\text{ZrO}_2\text{-P}$ (a) and $\text{Ni}/\text{ZrO}_2\text{-C}$ (b) catalysts.

4. Conclusions

In this work, the structural effect of Ni/ZrO₂ prepared via the DBD plasma decomposition of nickel nitrate has been investigated. The plasma decomposition, followed by the hydrogen reduction at 500 °C, leads to highly dispersed Ni/ZrO₂ with Ni(111) as the principally exposed facet and enhanced Ni-ZrO₂ interaction. The plasma decomposition also causes the formation of Ni-ZrO₂ interfacial sites with more oxygen vacancies, which play crucial roles in CO₂ activation and methanation. In addition, the plasma decomposed catalyst shows more efficient H₂ dissociation and hydrogen spillover from the Ni surface to carbonaceous species adsorbed on the strong basic sites of the ZrO₂. The high-coordinate Ni(111) with fewer defects facilitates the formate decomposition and CO hydrogenation. All these structural properties lead to a superior low temperature activity and almost 100% CH₄ selectivity in CO₂ methanation. It appears that CH₄ formation is limited by CO/formate hydrogenation, identified as the rate-limiting steps.

Acknowledgements

This work was supported by the National Key Research and Development Program of China (2016YFB0600902) and the National Natural Science Foundation of China (21536008, 21476157 and 21621004). The authors appreciate the helpful discussions with Prof. Qingfeng Ge at the Department of Chemistry of Southern Illinois University and Dr. Xinli Zhu at School of Chemical Engineering and Technology of Tianjin University.

Appendix A. Supplementary data

Supplementary material related to this article can be found, in the online version, at doi:<https://doi.org/10.1016/j.apcatb.2018.11.024>.

References

- [1] A. Kim, D.P. Debecker, F. Devred, V. Dubois, C. Sanchez, C. Sassoye, CO₂methanation on Ru/TiO₂ catalysts: On the effect of mixing anatase and rutile TiO₂ supports, *Appl. Catal. B: Environ.* 220 (2018) 615–625.
- [2] Y. Li, S.H. Chan, Q. Sun, Heterogeneous catalytic conversion of CO₂: a comprehensive theoretical review, *Nanoscale* 7 (2015) 8663–8683.
- [3] A. Solis-Garcia, J.F. Louvier-Hernandez, A. Almendarez-Camarillo, J.C. Pierro-Gonzalez, Participation of surface bicarbonate, formate and methoxy species in the carbon dioxide methanation catalyzed by ZrO₂-supported Ni, *Appl. Catal. B: Environ.* 218 (2017) 611–620.
- [4] W. Wang, J.L. Gong, Methanation of carbon dioxide: An overview, *Front. Chem. Sci. Eng.* 5 (2011) 2–10.
- [5] J. Xu, X. Su, H. Duan, B. Hou, Q. Lin, X. Liu, X. Pan, G. Pei, H. Geng, Y. Huang, T. Zhang, Influence of pretreatment temperature on catalytic performance of rutile TiO₂-supported ruthenium catalyst in CO₂ methanation, *J. Catal.* 333 (2016) 227–237.
- [6] D. Mateo, J. Albero, H. García, Graphene supported NiO/Ni nanoparticles as efficient photocatalyst for gas phase CO₂ reduction with hydrogen, *Appl. Catal. B: Environ.* 224 (2018) 563–571.
- [7] W. Li, X. Nie, X. Jiang, A. Zhang, F. Ding, M. Liu, Z. Liu, X. Guo, C. Song, ZrO₂ support imparts superior activity and stability of Co catalysts for CO₂ methanation, *Appl. Catal. B: Environ.* 220 (2018) 397–408.
- [8] I. Graça, L.V. González, M.C. Bacariza, A. Fernandes, C. Henriques, J.M. Lopes, M.F. Ribeiro, CO₂ hydrogenation into CH₄ on NiHNaUSY zeolites, *Appl. Catal. B: Environ.* 147 (2014) 101–110.
- [9] H. Peng, Y. Ma, W. Liu, X. Xu, X. Fang, J. Lian, X. Wang, C. Li, W. Zhou, P. Yuan, Methane dry reforming on Ni/La₂Zr₂O₇ treated by plasma in different atmospheres, *J. Energy Chem.* 24 (2015) 416–424.
- [10] R. Zhou, N. Rui, Z. Fan, C.-j. Liu, Effect of the structure of Ni/TiO₂ catalyst on CO₂ methanation, *Int. J. Hydrogen Energy* 41 (2016) 22017–22025.
- [11] F.D. Meylan, V. Moreau, S. Erkman, Material constraints related to storage of future European renewable electricity surpluses with CO₂ methanation, *Energy Policy* 94 (2016) 366–376.
- [12] Y. Yan, Y. Dai, Y. Yang, A.A. Lapkin, Improved stability of Y₂O₃ supported Ni catalysts for CO₂ methanation by precursor-determined metal-support interaction, *Appl. Catal. B: Environ.* 237 (2018) 504–512.
- [13] A. Vita, C. Italiano, L. Pino, P. Frontera, M. Ferraro, V. Antonucci, Activity and stability of powder and monolith-coated Ni/GDC catalysts for CO₂ methanation, *Appl. Catal. B: Environ.* 226 (2018) 384–395.
- [14] L. Xu, F. Wang, M. Chen, D. Nie, X. Lian, Z. Lu, H. Chen, K. Zhang, P. Ge, CO₂ methanation over rare earth doped Ni based mesoporous catalysts with intensified low-temperature activity, *Int. J. Hydrogen Energy* 42 (2017) 15523–15539.
- [15] Z. Fan, K. Sun, N. Rui, B. Zhao, C.-j. Liu, Improved activity of Ni/MgAl₂O₄ for CO₂ methanation by the plasma decomposition, *J. Energy Chem.* 24 (2015) 655–659.
- [16] C. Vogt, E. Groeneweld, G. Kamsma, M. Nachtegaal, L. Lu, C.J. Kiely, P.H. Berben, F. Meirer, B.M. Weckhuysen, Unravelling structure sensitivity in CO₂ hydrogenation over nickel, *Nat. Catal.* 1 (2018) 127–134.
- [17] M. Younas, L.L. Kong, M.J.K. Bashir, H. Nadeem, A. Shehzad, S. Sethupathi, Recent advancements, fundamental challenges, and opportunities in catalytic methanation of CO₂, *Energy Fuels* 30 (2016) 8815–8831.
- [18] G. Zhou, H. Liu, K. Cui, X. Zhai, G. Zhang, K. Xiong, X. Zheng, Methanation of carbon dioxide over Ni/CeO₂ catalysts: Effects of support CeO₂ structure, *Int. J. Hydrogen Energy* 42 (2017) 16108–16117.
- [19] X. Su, J. Xu, B. Liang, H. Duan, B. Hou, Y. Huang, Catalytic carbon dioxide hydrogenation to methane: A review of recent studies, *J. Energy Chem.* 25 (2016) 553–565.
- [20] J.C. Lavalle, Infrared spectrometric studies of the surface basicity of metal oxides and zeolites using adsorbed probe molecules, *Catal. Today* 27 (1996) 377–401.
- [21] L. Di, J. Zhang, X. Zhang, A review on the recent progress, challenges, and perspectives of atmospheric-pressure cold plasma for preparation of supported metal catalysts, *Plasma Process. Polym.* 15 (2018) e1700234.
- [22] C.-J. Liu, M. Li, J. Wang, X. Zhou, Q. Guo, J. Yan, Y. Li, Plasma methods for preparing green catalysts: Current status and perspective, *Chin. J. Catal.* 37 (2016) 340–348.
- [23] Z. Wang, Y. Zhang, E.C. Neyts, X. Cao, X. Zhang, B.W.L. Jang, C.-j. Liu, Catalyst preparation with plasmas: How does it work? *ACS Catal.* 8 (2018) 2093–2110.
- [24] X. Yan, B. Zhao, Y. Liu, Y. Li, Dielectric barrier discharge plasma for preparation of Ni-based catalysts with enhanced coke resistance: Current status and perspective, *Catal. Today* 256 (2015) 29–40.
- [25] X. Yan, Y. Liu, B. Zhao, Y. Wang, C.-J. Liu, Enhanced sulfur resistance of Ni/SiO₂ catalyst for methanation via the plasma decomposition of nickel precursor, *Phys. Chem. Chem. Phys.* 15 (2013) 12132–12138.
- [26] X. Yan, Y. Liu, B. Zhao, Z. Wang, Y. Wang, C.-J. Liu, Methanation over Ni/SiO₂: Effect of the catalyst preparation methodologies, *Int. J. Hydrogen Energy* 38 (2013) 2283–2291.
- [27] X. Guo, Y. Sun, Y. Yu, X. Zhu, C.-j. Liu, Carbon formation and steam reforming of methane on silica supported nickel catalysts, *Catal. Commun.* 19 (2012) 61–65.
- [28] Y. Zhang, W. Wang, Z. Wang, X. Zhou, Z. Wang, C.-J. Liu, Steam reforming of methane over Ni/SiO₂ catalyst with enhanced coke resistance at low steam to methane ratio, *Catal. Today* 256 (2015) 130–136.
- [29] K. Ray, G. Deo, A potential descriptor for the CO₂ hydrogenation to CH₄ over Al₂O₃ supported Ni and Ni-based alloy catalysts, *Appl. Catal. B: Environ.* 218 (2017) 525–537.
- [30] M. Boudart, Turnover rates in heterogeneous catalysis, *Chem. Rev.* 95 (1995) 661–666.
- [31] Q. Liu, X. Dong, X. Mo, W. Lin, Selective catalytic methanation of CO in hydrogen-rich gases over Ni/ZrO₂ catalyst, *J. Nat. Gas Chem.* 17 (2008) 268–272.
- [32] M.M.V.M. Souza, D.A.G. Aranda, M. Schmal, Reforming of methane with carbon dioxide over Pt/ZrO₂/Al₂O₃ catalysts, *J. Catal.* 204 (2001) 498–511.
- [33] J.H. Bitter, K. Seshan, J.A. Lercher, The state of zirconia supported platinum catalysts for CO₂/CH₄ reforming, *J. Catal.* 171 (1997) 279–286.
- [34] M.C.J. Bradford, M.A.V. Vannice, Metal-support interactions during the CO₂ reforming of CH₄ over model TiO_x/Pt catalysts, *Catal. Lett.* 48 (1997) 31–38.
- [35] X.S. Li, W.Z. Li, Y.X. Chen, H.L. Wang, Enhancement of hydrogen spillover by surface labile oxygen species on oxidized Pt/TiO₂ catalyst, *Catal. Lett.* 32 (1995) 31–42.
- [36] B. Bachiller-Baeza, I. Rodriguez-Ramos, A. Guerrero-Ruiz, Interaction of carbon dioxide with the surface of zirconia polymorphs, *Langmuir* 14 (1998) 3556–3564.
- [37] H. Takano, H. Shinomiya, K. Izumiya, N. Kumagai, H. Habazaki, K. Hashimoto, CO₂ methanation of Ni catalysts supported on tetragonal ZrO₂ doped with Ca²⁺ and Ni²⁺ ions, *Int. J. Hydrogen Energy* 40 (2015) 8347–8355.
- [38] N. Rui, Z. Wang, K. Sun, J. Ye, Q. Ge, C.-j. Liu, CO₂ hydrogenation to methanol over Pd/In₂O₃: Effects of Pd and oxygen vacancy, *Appl. Catal. B: Environ.* 218 (2017) 488–497.
- [39] M. Romero-Sáez, A.B. Dongil, N. Benito, R. Espinoza-González, N. Escalona, F. Gracia, CO₂ methanation over nickel-ZrO₂ catalyst supported on carbon nanotubes: A comparison between two impregnation strategies, *Appl. Catal. B: Environ.* 237 (2018) 817–825.
- [40] A. Quindimil, U. De-La-Torre, B. Pereda-Ayo, J.A. González-Marcos, J.R. González-Velasco, Ni catalysts with La as promoter supported over Y- and BETA-zeolites for CO₂ methanation, *Appl. Catal. B: Environ.* 238 (2018) 393–403.
- [41] M. Yamasaki, H. Habazaki, K. Asami, K. Izumiya, K. Hashimoto, Effect of tetragonal ZrO₂ on the catalytic activity of Ni/ZrO₂ catalyst prepared from amorphous Ni-Zr alloys, *Catal. Commun.* 7 (2006) 24–28.
- [42] K. Pokrovski, K.T. Jung, A.T. Bell, Investigation of CO and CO₂ adsorption on tetragonal and monoclinic zirconia, *Langmuir* 17 (2001) 4297–4303.
- [43] Q. Pan, J. Peng, T. Sun, S. Wang, S. Wang, Insight into the reaction route of CO₂ methanation: Promotion effect of medium basic sites, *Catal. Commun.* 45 (2014) 74–78.
- [44] C. Drouilly, J.-M. Krafft, F. Averseng, H. Lauron-Pernot, D. Bazer-Bachi, C. Chizallet, V. Lecocq, G. Costentin, Role of oxygen vacancies in the basicity of ZnO: from the model methylbutynol conversion to the ethanol transformation application, *Appl. Catal. A Gen.* 453 (2013) 121–129.
- [45] L. Yang, L. Pastor-Pérez, S. Gu, A. Sepúlveda-Escribano, T.R. Reina, Highly efficient Ni/CeO₂-Al₂O₃ catalysts for CO₂ upgrading via reverse water-gas shift: Effect of selected transition metal promoters, *Appl. Catal. B: Environ.* 232 (2018) 464–471.
- [46] C. Heine, B.A.J. Lechner, H. Bluhm, M. Salmeron, Recycling of CO₂: Probing the

- chemical state of the Ni(111) surface during the methanation reaction with ambient-pressure X ray photoelectron spectroscopy, *J. Am. Chem. Soc.* 138 (2016) 13246–13252.
- [47] I. Czekaj, F. Loviat, F. Raimondi, J. Wambach, S. Biollaz, A. Wokaun, Characterization of surface processes at the Ni-based catalyst during the methanation of biomass-derived synthesis gas: X-ray photoelectron spectroscopy (XPS), *Appl. Catal. A Gen.* 329 (2007) 68–78.
- [48] M. Németh, Z. Schay, D. Sránkó, J. Károlyi, G. Sáfrán, I. Sajó, A. Horváth, Impregnated Ni/ZrO₂ and Pt/ZrO₂ catalysts in dry reforming of methane: Activity tests in excess methane and mechanistic studies with labeled ¹³CO₂, *Appl. Catal. A Gen.* 504 (2015) 608–620.
- [49] J.G. Tao, J.S. Pan, C.H.A. Huan, Z. Zhang, J.W. Chai, S.J. Wang, Origin of XPS binding energy shifts in Ni clusters and atoms on rutile TiO₂ surfaces, *Surf. Sci.* 602 (2008) 2769–2773.
- [50] M.A. Rahman, S. Rout, J.P. Thomas, D. McGillivray, K.T. Leung, Defect-rich dopant-free ZrO₂ nanostructures with superior dilute ferromagnetic semiconductor properties, *J. Am. Chem. Soc.* 138 (2016) 11896–11906.
- [51] K.-Y. Lee, Y.-J. Huang, Low CO generation on tunable oxygen vacancies of non-precious metallic Cu/ZnO catalysts for partial oxidation of methanol reaction, *Appl. Catal. B: Environ.* 150–151 (2014) 506–514.
- [52] S. Collins, M. Baltanas, A. Bonivardi, An infrared study of the intermediates of methanol synthesis from carbon dioxide over Pd/β-Ga₂O₃, *J. Catal.* 226 (2004) 410–421.
- [53] S.T. Korhonen, M. Calatayud, A.O.I. Krause, Structure and stability of formates and carbonates on monoclinic zirconia: A combined study by density functional theory and infrared spectroscopy, *J. Phys. Chem. C* 112 (2008) 16096–16102.
- [54] P.A.U. Aldana, F. Ocampo, K. Kobl, B. Louis, F. Thibault-Starzyk, M. Daturi, P. Bazin, S. Thomas, A.C. Roger, Catalytic CO₂ valorization into CH₄ on Ni-based ceria-zirconia. Reaction mechanism by operando IR spectroscopy, *Catal. Today* 215 (2013) 201–207.
- [55] M. Marwood, R. Doepper, A. Renken, In-situ surface and gas phase analysis for kinetic studies under transient conditions The catalytic hydrogenation of CO₂, *Appl. Catal. A Gen.* 151 (1997) 223–246.
- [56] A. Westermann, B. Azambre, M.C. Bacariza, I. Graça, M.F. Ribeiro, J.M. Lopes, C. Henriques, Insight into CO₂ methanation mechanism over NiUSY zeolites: An operando IR study, *Appl. Catal. B: Environ.* 174–175 (2015) 120–125.
- [57] J. Ren, H. Guo, J. Yang, Z. Qin, J. Lin, Z. Li, Insights into the mechanisms of CO₂ methanation on Ni(111) surfaces by density functional theory, *Appl. Surf. Sci.* 351 (2015) 504–516.
- [58] S.J. Choe, H.J. Kang, S.-J. Kim, S.-B. Park, D.H. Park, D.S. Huh, Adsorbed carbon formation and carbon hydrogenation for CO₂ methanation on the Ni(111) surface: ASEED-MO study, *Bull. Korean Chem. Soc.* 26 (2005) 1682–1688.
- [59] H.C. Wu, Y.C. Chang, J.H. Wu, J.H. Lin, I.K. Lin, C.S. Chen, Methanation of CO₂ and reverse water gas shift reactions on Ni/SiO₂ catalysts: the influence of particle size on selectivity and reaction pathway, *Catal. Sci. Technol.* 5 (2015) 4154–4163.
- [60] P. Shi, C.-J. Liu, Characterization of silica supported nickel catalyst for methanation with improved activity by room temperature plasma treatment, *Catal. Lett.* 133 (2009) 112–118.
- [61] X. Xie, Y. Li, Z.-Q. Liu, M. Haruta, W. Shen, Low-temperature oxidation of CO catalysed by Co₃O₄ nanorods, *Nature* 458 (2009) 746–749.